Batteries Hot Paper

How to cite: *Angew. Chem. Int. Ed.* **2021**, *60*, 22189–22194
International Edition: doi.org/10.1002/anie.202107697
German Edition: doi.org/10.1002/ange.202107697

Construction of Co–Mn Prussian Blue Analog Hollow Spheres for Efficient Aqueous Zn-ion Batteries

*Yinxiang Zeng, Xue Feng Lu, Song Lin Zhang, Deyan Luan, Sheng Li, and Xiong Wen (David) Lou**

Abstract: *Prussian blue analogs (PBAs) are considered as reliable and promising cathode materials for aqueous Zn-ion batteries (AZIBs), but they suffer from low capacity and poor cycling stability due to insufficient active sites and structural damage caused by the ion insertion/extraction processes. Herein, a template-engaged ion exchange approach has been developed for the synthesis of Co-substituted Mn-rich PBA hollow spheres (CoMn-PBA HSs) as cathode materials for AZIBs. Benefiting from the multiple advantageous features including hollow structure, abundant active sites, fast Zn^{2+} ion diffusion, and partial Co substitution, the CoMn-PBA HSs electrode shows efficient zinc ion storage properties in terms of high capacity, decent rate capability and prolonged cycle life.*

Aqueous Zn-ion batteries (AZIBs) are emerging as one of the most promising candidates for efficient grid-scale storage of renewable but intermittent energy sources, due to their significant merits of high safety, cost-effectiveness, simplified manufacture, and high ionic conductivity of water-based electrolytes (up to 1 $S\,cm^{-1}$).[1–4] Moreover, the Zn anode could offer high theoretical capacity (840 $mAh\,g^{-1}$) and low electrochemical potential (−0.76 V versus standard hydrogen electrode), making AZIBs more attractive.[5–8] In recent years, tremendous efforts have been dedicated to exploring and designing efficient cathode materials for AZIBs, such as Prussian blue analogs (PBAs),[9,10] Mn-based compounds,[11,12] and V-based compounds.[13,14] Among them, PBAs have attracted widespread attention in view of their appealing features including three-dimensional open frameworks, high stability against water, and multiple active sites.[10,15–17] The cubic crystal structure of PBAs contains an open ion channel with a diameter of 3.2 Å in the (100) direction and large interstitial nanocavities with a diameter of 4.6 Å, thus ensuring the efficient Zn^{2+} ion insertion/extraction.[18,19] In particular, Mn-PBAs characterized by a high theoretical capacity and high output voltage hold great promise as compelling cathodes for AZIBs.[20–22] In Mn-PBAs, both Fe and Mn are redox-active sites and can provide extra capacity by redox reaction during the charge–discharge processes.[18,25] However, the cycling stability of Mn-PBAs is far from satisfactory owing to the structural deformation caused by the Jahn–Teller distortion and severe volume variation during the ion insertion/extraction processes.[23,24]

To address these issues, strategies including morphology design, metal substitution, and electrolyte optimization have been demonstrated to extend the lifespan of Mn-PBAs.[25–28] For example, constructing hollow structures has been proved as a feasible approach to effectively alleviate the structural strain during the ion insertion/extraction processes and boost the stability of PBAs.[29–31] Moreover, Jiang et al. reported that Fe-substitution could decrease the density of Mn^{3+} ions in the lattice and mitigate the phase transitions of Mn-PBAs, which remarkably improved its cycling performance.[32] Ni or Co substituted Mn-PBAs also showed enhanced durability by the suppression of the Jahn–Teller distortion of Mn^{3+} ions.[33–35] Thus, it is highly desirable to integrate these strategies into one system to promote the electrochemical properties of Mn-PBAs for AZIBs.

Herein, we develop an efficient self-templating strategy for the construction of Co-substituted Mn-rich PBA hollow spheres (denoted as CoMn-PBA HSs) through a facile anion exchange process. First, CoMn-glycerate solid spheres (SSs) are prepared as the precursor, followed by a one-step ion exchange reaction to obtain CoMn-PBA HSs. The hollow structure can not only provide large surface area and sufficient active sites but also accommodate the large volume change during the repeated charge–discharge processes. Furthermore, Co substitution will further stabilize the crystal structure of CoMn-PBA HSs and boost the cycle life. As expected, the as-prepared CoMn-PBA HSs exhibit high reversible capacity, favorable rate performance, and impressive cycling stability when employed as a cathode for AZIBs.

The synthesis process of CoMn-PBA HSs is illustrated in Figure 1a. CoMn-glycerate SSs prepared through a facile solvothermal method are adopted as the self-templating precursor (see the experimental details in Supporting Information (SI)).[36] Field-emission scanning electron microscopy (FESEM) images show that the as-prepared CoMn-glycerate SSs are uniform with an average diameter of about 900 nm

[*] Prof. S. Li
Department of Physics, Zhejiang Normal University
Jinhua City, Zhejiang Province, 321004 (P. R. China)
Dr. Y. X. Zeng, Dr. X. F. Lu, S. L. Zhang, Dr. D. Y. Luan, Prof. X. W. Lou
School of Chemical and Biomedical Engineering, Nanyang Technological University
62 Nanyang Drive, Singapore, 637459 (Singapore)
E-mail: xwlou@ntu.edu.sg
davidlou88@gmail.com
Homepage: https://personal.ntu.edu.sg/xwlou/
Supporting information and the ORCID identification number(s) for the author(s) of this article can be found under: https://doi.org/10.1002/anie.202107697.

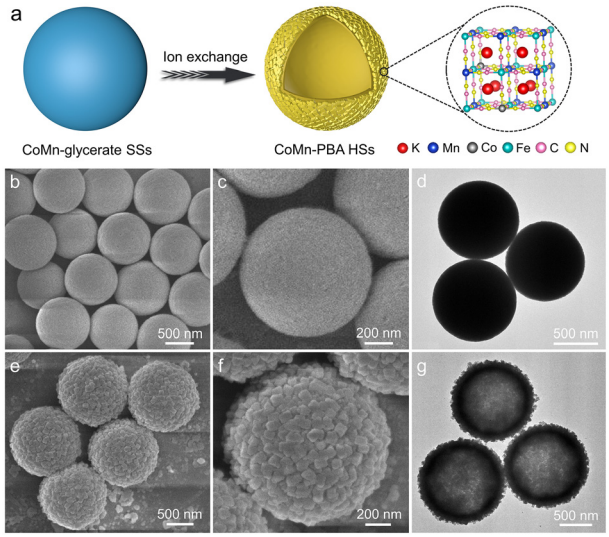

Figure 1. a) The synthetic process of CoMn-PBA HSs. b,c,e,f) FESEM and d,g) TEM images of b–d) CoMn-glycerate SSs and e–g) CoMn-PBA HSs.

(Figure 1b,c; Figure S1a, SI). Transmission electron microscopy (TEM) images further demonstrate the solid nature and smooth surface of CoMn-glycerate SSs (Figure 1d; Figure S1b, SI). Subsequently, the as-prepared CoMn-glycerate SSs are converted to CoMn-PBA HSs through an anion exchange process (see the experimental details in SI). FESEM images reveal that CoMn-PBA HSs still maintain the sphere-like morphology but the surface becomes rough (Figure 1e; Figure S2a, SI). A close observation discloses the hierarchical structure of the spheres with nanocube subunits on the surface (Figure 1f). TEM images confirm the hollow structure with a hierarchical surface for CoMn-PBA HSs (Figure 1g; Figure S2b, SI). The diameter of CoMn-PBA HSs is increased to about 1.2 μm because of the formation of nanocube subunits on the surface.

A typical TEM image of an individual CoMn-PBA HS further demonstrates the well-defined hollow structure with a shell thickness of about 200 nm (Figure 2a). The enlarged view of an individual CoMn-PBA HS shows that the exterior surface is assembled by nanocubes with an average size of about 70 nm (Figure 2b). In the high-resolution TEM (HRTEM) images, two distinct lattice fringes with interplanar spacings of 0.35 and 0.50 nm can be clearly observed, which correspond to the (220) and (020) planes of KMnFe(CN)$_6$·nH$_2$O (JCPDS card No. 51-1896), respectively (Figure 2c,d). The high-angle annular dark-field scanning transmission electron microscopy (HAADF-STEM) image and the corresponding elemental mapping images of an individual CoMn-PBA HS indicate the uniform distribution of C, N, K, Mn, Co, Fe elements (Figure 2e).

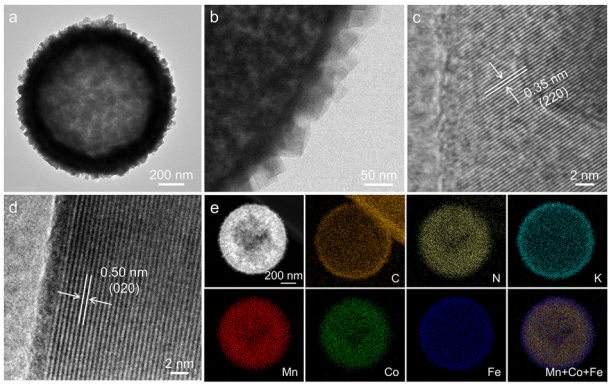

Figure 2. a,b) TEM and c,d) HRTEM images, e) HAADF-STEM image and the elemental mapping images of an individual CoMn-PBA HS.

The X-ray diffraction (XRD) pattern of CoMn-glycerate SSs shows an obvious broad peak at around 12°, which is consistent with the characteristic peak of metal alkoxides (Figure 3a).[37,38] All diffraction peaks of CoMn-PBA HSs can be indexed to the monoclinic phase of KMnFe(CN)$_6$·nH$_2$O (JCPDS card No. 51-1896). No diffraction peaks of residues or other impurities are detected, suggesting that CoMn-glycerate SSs are completely converted to CoMn-PBA HSs. According to the inductively coupled plasma atomic emission spectroscopy (ICP-AES) results, the elemental composition of CoMn-PBA HSs is determined to be $K_{1.34}Co_{0.23}Mn_{0.88}[Fe(CN)_6]$. The energy-dispersive X-ray (EDX) analysis of CoMn-glycerate SSs verifies the presence of C, O, Mn, Co elements with the Co to Mn atomic ratio of about 1:3.8 (Figure S3a, SI). After the ion exchange reaction, the EDX spectrum of obtained CoMn-PBA HSs confirms the chemical composition of C, N, O, K, Mn, Co, Fe elements, and the atomic ratio of Co to Mn remains almost unchanged (Figure S3b, SI). The chemical structure of CoMn-glycerate SSs and CoMn-PBA HSs is further investigated by Fourier-transform infrared (FTIR) spectroscopy (Figure S4, SI). For CoMn-PBA HSs, the strong peak located at 2066 cm^{-1} corresponds to the typical C≡N stretching vibration and the peak at 594 cm^{-1} is attributed to the vibration mode of Fe–C.[21,39] Additionally, the weak peak at 1633 cm^{-1} and the broad peak at 3439 cm^{-1} could be associated with the H-O-H bending vibration and O-H stretching vibration of H_2O, respectively.[40,41] No peaks of CoMn-glycerate SSs can be recognized in the FTIR spectrum of CoMn-PBA HSs, validating the complete and successful transformation of CoMn-glycerate SSs into CoMn-PBA HSs. To further explore the surface chemical states of CoMn-PBA HSs, X-ray photoelectron spectroscopy (XPS) analysis is carried out. The survey spectrum reveals that CoMn-PBA HSs contain C, N, O, K, Mn, Co, Fe elements and no other impurities (Figure S5, SI), which agrees well with the EDX results. The high-resolution XPS spectrum of Fe 2p shows two peaks at 708.2 and 720.9 eV, representing the characteristic Fe^{2+} $2p_{3/2}$ and Fe^{2+} $2p_{1/2}$ peaks, respectively (Figure 3b).[20] The Mn 2p spectrum can be well deconvoluted into two pairs of peaks attributed to Mn^{2+} and Mn^{3+} (Figure 3c), suggesting the existence of both Mn^{2+} and Mn^{3+} in CoMn-PBA HSs, which is consistent with Mn-PBA HSs (Figure S6a, SI).[21,42] In addition to two satellite peaks, there are another two peaks located at 780.8 and 796.7 eV in the Co 2p spectrum, which correspond to $2p_{3/2}$ and $2p_{1/2}$ peaks of Co^{2+}, respectively (Figure 3d).[43,44] The valence state of Co in Co-PBA HSs is also +2 (Figure S6b, SI). All these characterizations and

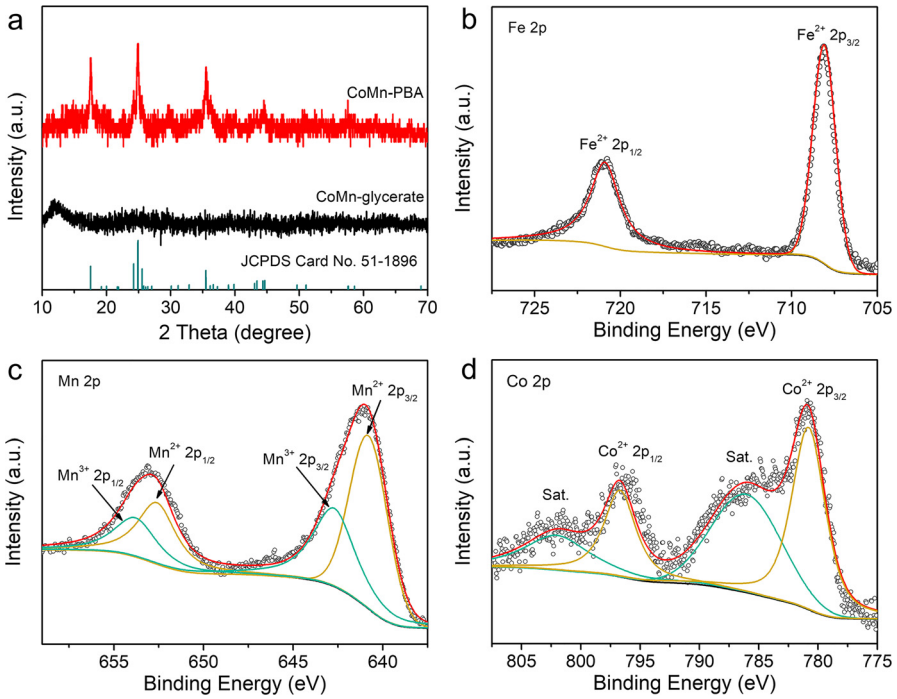

Figure 3. a) XRD patterns of CoMn-glycerate SSs and CoMn-PBA HSs. High-resolution XPS spectra of b) Fe 2p, c) Mn 2p, d) Co 2p for CoMn-PBA HSs.

analyses comprehensively confirm the successful synthesis of CoMn-PBA HSs through a self-templating approach.

This self-templating strategy is further extended to synthesize Mn-PBA HSs and Co-PBA HSs. Similarly, Mn-glycerate and Co-glycerate SSs are prepared by the solvothermal method as the self-templating precursors (see the experimental details in SI). FESEM and TEM images reveal the slightly rough surface with small nanoparticles and solid interior for Mn-glycerate SSs (Figure S7, SI). After the ion exchange reaction, Mn-PBA HSs display the well-defined hollow structure with a nanocube-assembled surface (Figure S8, SI). All the peaks of Mn-PBA HSs in the XRD pattern match well with the standard peaks of $KMnFe(CN)_6 \cdot n\,H_2O$ (Figure S9, SI), which is consistent with the result of CoMn-PBA HSs. ICP-AES results show that the elemental compositions of Mn-PBA HSs and Co-PBA HSs are $K_{1.45}Mn_{1.08}[Fe(CN)_6]$ and $K_{1.97}Co_{1.15}[Fe(CN)_6]$, respectively. EDX analyses also indicate the transformation of Mn-glycerate SSs into Mn-PBA HSs (Figure S10, SI). FESEM and TEM images of Co-glycerate SSs demonstrate their solid nature and relatively smooth surface (Figure S11, SI). Interestingly, the as-obtained Co-PBA HSs present a double-shelled hollow structure with a visible gap between the outer and inner shells (Figure S12, SI). The average thickness of the outer and inner shells is about 100 and 150 nm, respectively. Based on the XRD patterns and EDX results, all Co-glycerate SSs are successfully converted into Co-PBA HSs (Figure S13 and S14, SI). Furthermore, thermogravimetric analysis (TGA) results show that the coordinated water contents are about 7.1%, 5.4%, 16.9% for CoMn-PBA HSs, Mn-PBA HSs, Co-PBA HSs, respectively (Figure S15, SI). The low content of coordinated water will leave more channels for ion insertion and thus benefit the zinc ion storage.[18,25] Nitrogen sorption isotherms (Figure S16, SI) reveal that CoMn-PBA HSs possess a Brunauer-Emmett-Teller (BET) specific surface area of 89.8 $m^2 g^{-1}$, which is much higher than that of Mn-PBA HSs (46.3 $m^2 g^{-1}$) and Co-PBA HSs (35.8 $m^2 g^{-1}$).

The electrochemical performance of CoMn-PBA HSs, Mn-PBA HSs, and Co-PBA HSs is evaluated as cathode materials for AZIBs. Before test, all the batteries are activated at 0.02 A g^{-1} for 1 cycle. K 2p XPS spectra of pristine, charged, and discharged CoMn-PBA HSs reveal that K^+ ions are fully extracted during the first charge process and there is no intercalation/deintercalation behavior of K^+ ions in the following cycles (Figure S17, SI). As shown in Figure 4a, the CoMn-PBA HSs electrode possesses a similar cyclic voltammetry (CV) curve as that of the Mn-PBA HSs electrode, both of which display three pairs of obvious redox peaks, suggesting that the introduction of Co into Mn-PBA has little influence on the surface electrochemical reaction. While the Co-PBA HSs electrode shows two poorly defined pairs of redox peaks with much lower current density, indicative of the inferior electrochemical reaction activity. From previous studies,[20,32] Zn^{2+} ions are inserted into the tunnels of CoMn-PBA HSs during the discharge process, accompanied by the formation of monoclinic phase. Zn^{2+} ions are reversibly deinserted and the phase transition from monoclinic to cubic happens during the charge process. Thus, the chemical reaction of CoMn-PBA HSs could be formulated as following:

$K_{1.34}Co_{0.23}Mn_{0.88}[Fe(CN)_6] - 1.34\,e^- \rightarrow Co_{0.23}Mn_{0.88}[Fe(CN)_6] + 1.34\,K^+$ (first charge), $Co_{0.23}Mn_{0.88}[Fe(CN)_6] + x\,Zn^{2+} + 2x\,e^- \leftrightarrow Zn_xCo_{0.23}Mn_{0.88}[Fe(CN)_6]$ (next cycles).

Figure 4b compares the galvanostatic discharge-charge voltage profiles of the CoMn-PBA HSs, Mn-PBA HSs, and Co-PBA HSs electrodes at a current density of 0.05 A g^{-1}. The CoMn-PBA HSs electrode exhibits a longer discharge plateau than Mn-PBA HSs and Co-PBA HSs electrodes, confirming the best charge storage performance of the CoMn-PBA HSs electrode. Specifically, an impressive capacity of 128.6 mAh g^{-1} is achieved by the CoMn-PBA HSs electrode, which is significantly higher than that of Mn-PBA HSs (85.9 mAh g^{-1}) and Co-PBA HSs (45.5 mAh g^{-1}) electrodes, as well as most reported PBA-based cathodes for aqueous rechargeable batteries (Table S1, SI).[10,16,20,27,28] Even when the current density increases to 2 A g^{-1}, the CoMn-PBA HSs electrode still retains a capacity of 50.4 mAh g^{-1} (Figure 4c), which outperforms the Mn-PBA HSs (36.8 mAh g^{-1}) and Co-PBA HSs (19.7 mAh g^{-1}) electrodes (Figure S18, SI). Furthermore, the rate performance of CoMn-PBA HSs, Mn-PBA

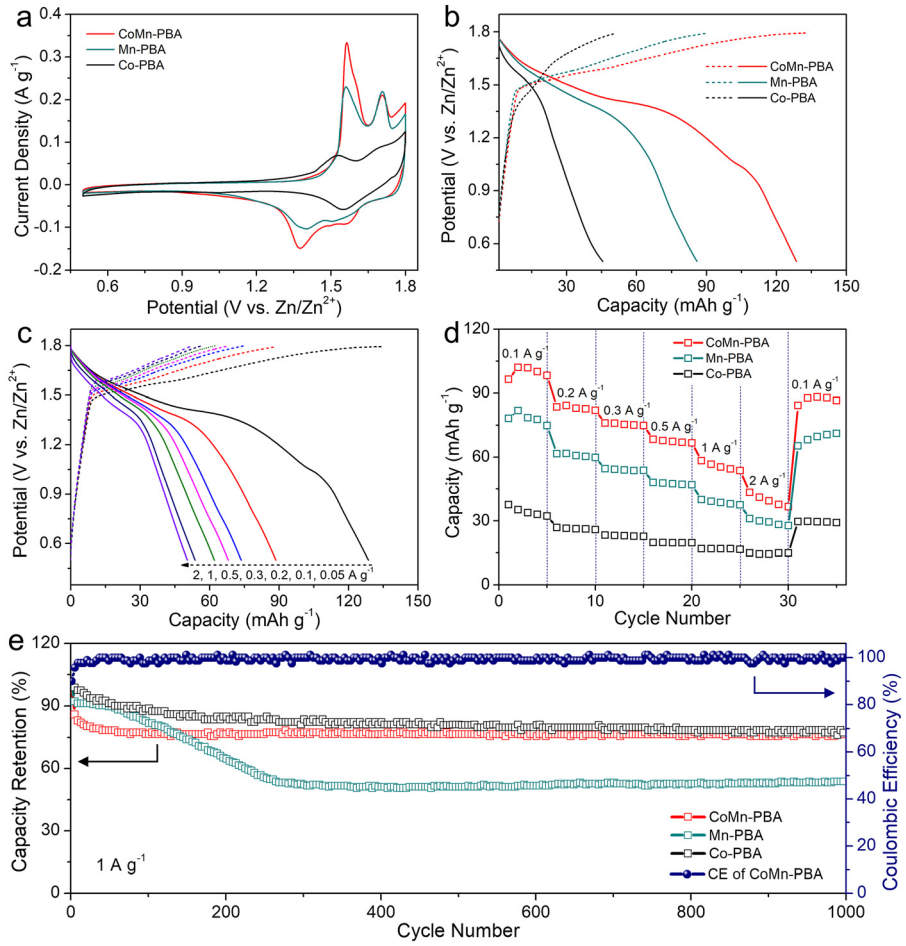

Figure 4. a) CV curves at a scan rate of 0.2 mV s^{-1}, b) charge–discharge voltage profiles at a current density of 0.05 A g^{-1} of CoMn-PBA HSs, Mn-PBA HSs, and Co-PBA HSs electrodes. c) Charge–discharge voltage profiles of the CoMn-PBA HSs electrode at various current densities. d) Rate performance based on discharging curves and e) cycling performance tested at a current density of 1 A g^{-1} of CoMn-PBA HSs, Mn-PBA HSs, and Co-PBA HSs electrodes.

HSs, and Co-PBA HSs is also investigated at various current densities (Figure 4d). The CoMn-PBA HSs electrode delivers average discharge capacities of 99.7, 83.1, 75.4, 67.4, 55.7, 39.7 mAh g^{-1} at the current densities of 0.1, 0.2, 0.3, 0.5, 1, 2 A g^{-1}, respectively. Moreover, an average reversible capacity of 86.9 mAh g^{-1} can be recovered as the current density is reduced back to 0.1 A g^{-1}, indicating the superior rate property. For comparison, the Mn-PBA HSs and Co-PBA HSs electrodes afford much lower capacities at the same current densities (Figure 4d). The superior capacity of CoMn-PBA HSs over Co-PBA HSs and Mn-PBA HSs might be ascribed to their higher specific surface area, sufficient active sites, and low content of coordinated water.

Figure 4e displays the long-term cycling performance of CoMn-PBA HSs, Mn-PBA HSs, and Co-PBA HSs at 1 A g^{-1}. The capacity of the Mn-PBA HSs electrode decreases rapidly in the first 300 cycles and retains 53.6% of the initial capacity after 1000 cycles. In contrast, the CoMn-PBA HSs electrode exhibits superior cycling stability with a capacity retention of 76.4% over 1000 cycles. The Coulombic efficiency (CE) of the CoMn-PBA HSs electrode is always approaching 100% during the cycling processes, manifesting its high reaction reversibility. Moreover, the cycling performance of CoMn-PBA HSs and Mn-PBA HSs electrodes at 2 A g^{-1} again proves the improved durability of the CoMn-PBA HSs electrode brought by Co substitution (Figure S19, SI). The structure and composition of the CoMn-PBA HSs electrode are well preserved after 1000 cycles, further evidencing the excellent stability of CoMn-PBA HSs (Figure S20, SI). The capacity decay of Mn-PBA HSs might be originated from the Jahn–Teller distortion induced structural deformation of Mn-N_6 octahedra upon Zn^{2+} ion insertion/extraction, which will further lead to the dissolution of active materials in the electrolyte.[23,24] A small amount of Co substitution in the CoMn-PBA HSs electrode could mitigate the Jahn–Teller distortion and stabilize the crystal structure, thus enabling a prolonged cycle life.[33,34] The charge storage kinetics of the CoMn-PBA HSs electrode is explored by CV curves at different scan rates (Figure S21a, SI). According to the power-law relationship, the peak current (i) and scan rate (v) obey this equation: $i = a v^b$.[45] Generally, a b value close to 0.5 represents the diffusion-controlled process, and a b value close to 1 means mainly capacitive-controlled behavior.[46] The b values are all higher than 0.75 for the two pairs of redox peaks, suggesting that the corresponding reactions at the peak regions follow dominantly fast capacitive-controlled behavior for the CoMn-PBA HSs electrode (Figure S21b, SI).

We have also investigated the electrochemical performance of CoMn-PBA HSs with different Co/Mn atomic ratios. The CoMn-PBA HSs electrode with a Co/Mn atomic ratio of 1:4 exhibits the optimized zinc ion storage performance in terms of capacity and cyclic stability (Figure S22, SI). Moreover, all the CoMn-PBA HSs electrodes present better cycling performance than the Mn-PBA HSs electrode, revealing that Co substitution could improve the structural stability of Mn-PBAs. To verify the advantages of the hollow structure with thin shell, CoMn-PBA nanocubes (NCs) and CoMn-PBA HSs with thick shell are synthesized and employed as control samples. Evidently, the CoMn-PBA HSs electrode with thin shell shows better zinc ion storage performance than two control samples (Figure S23–25, SI). The efficient zinc ion storage properties of CoMn-PBA HSs could be attributed to the hierarchical hollow structure and

compositional advantages. Specifically, the hollow configuration can effectively accommodate the mechanical strain induced by the Zn^{2+} ion insertion/extraction during cycling. And the Co substitution in CoMn-PBA HSs might suppress the Jahn–Teller distortion and mitigate structural damage. As a result, improved cycling stability and reaction reversibility are realized by this CoMn-PBA HSs electrode. Besides, the thin shell and nanocube subunits can provide rich active sites and fast Zn^{2+} ion diffusion, thus enabling high capacity and fast reaction kinetics.

In summary, we report a self-templating method for the rational synthesis of CoMn-PBA HSs as cathode materials for AZIBs. Using CoMn-glycerate SSs as the precursor, CoMn-PBA HSs are facilely obtained by the anion exchange reaction between CoMn-glycerates and $[Fe(CN)_6]^{4-}$ ions under reflux condition. Owing to the beneficial hollow structure and partial Co substitution, the CoMn-PBA HSs electrode exhibits enhanced zinc ion storage performance with a high reversible capacity (128.6 $mAh\,g^{-1}$ at 0.05 $A\,g^{-1}$), good rate capability (50.4 $mAh\,g^{-1}$ at 2 $A\,g^{-1}$), as well as impressive cycling performance (76.4% capacity retention over 1000 cycles). This work may give some inspiration for the design and synthesis of advanced cathode materials for AZIBs.

Acknowledgements

X.W.L. acknowledges the funding support from the Ministry of Education of Singapore through the Academic Research Fund (AcRF) and Tier-2 grants (MOE2017-T2-2-003; MOE2019-T2-2-049).

Conflict of Interest

The authors declare no conflict of interest.

Keywords: Co substitution · hollow spheres · ion exchange · Prussian blue analogs · Zn-ion batteries

[1] L. Cao, D. Li, T. Pollard, T. Deng, B. Zhang, C. Yang, L. Chen, J. Vatamanu, E. Hu, M. J. Hourwitz, L. Ma, M. Ding, Q. Li, S. Hou, K. Gaskell, J. T. Fourkas, X. Q. Yang, K. Xu, O. Borodin, C. Wang, *Nat. Nanotechnol.* **2021**, https://doi.org/10.1038/s41565-021-00905-4.
[2] N. Zhang, X. Chen, M. Yu, Z. Niu, F. Cheng, J. Chen, *Chem. Soc. Rev.* **2020**, *49*, 4203.
[3] L. E. Blanc, D. Kundu, L. F. Nazar, *Joule* **2020**, *4*, 771.
[4] H. Pan, Y. Shao, P. Yan, Y. Cheng, K. S. Han, Z. Nie, C. Wang, J. Yang, X. Li, P. Bhattacharya, K. T. Mueller, J. Liu, *Nat. Energy* **2016**, *1*, 16039.
[5] F. Wang, O. Borodin, T. Gao, X. Fan, W. Sun, F. Han, A. Faraone, J. A. Dura, K. Xu, C. Wang, *Nat. Mater.* **2018**, *17*, 543.
[6] J. Zheng, L. A. Archer, *Sci. Adv.* **2021**, *7*, eabe0219.
[7] L. Cao, D. Li, E. Hu, J. Xu, T. Deng, L. Ma, Y. Wang, X. Q. Yang, C. Wang, *J. Am. Chem. Soc.* **2020**, *142*, 21404.
[8] Y. Zeng, X. Zhang, R. Qin, X. Liu, P. Fang, D. Zheng, Y. Tong, X. Lu, *Adv. Mater.* **2019**, *31*, 1903675.
[9] L. Ma, S. Chen, C. Long, X. Li, Y. Zhao, Z. Liu, Z. Huang, B. Dong, J. A. Zapien, C. Zhi, *Adv. Energy Mater.* **2019**, *9*, 1902446.
[10] C. Liu, X. Wang, W. Deng, C. Li, J. Chen, M. Xue, R. Li, F. Pan, *Angew. Chem. Int. Ed.* **2018**, *57*, 7046; *Angew. Chem.* **2018**, *130*, 7164.
[11] C. Zhong, B. Liu, J. Ding, X. Liu, Y. Zhong, Y. Li, C. Sun, X. Han, Y. Deng, N. Zhao, W. Hu, *Nat. Energy* **2020**, *5*, 440.
[12] N. Zhang, F. Cheng, J. Liu, L. Wang, X. Long, X. Liu, F. Li, J. Chen, *Nat. Commun.* **2017**, *8*, 405.
[13] L. Wang, K. W. Huang, J. Chen, J. Zheng, *Sci. Adv.* **2019**, *5*, eaax4279.
[14] S. Liu, H. Zhu, B. Zhang, G. Li, H. Zhu, Y. Ren, H. Geng, Y. Yang, Q. Liu, C. C. Li, *Adv. Mater.* **2020**, *32*, 2001113.
[15] X. Wu, J. J. Hong, W. Shin, L. Ma, T. Liu, X. Bi, Y. Yuan, Y. Qi, T. W. Surta, W. Huang, J. Neuefeind, T. Wu, P. A. Greaney, J. Lu, X. Ji, *Nat. Energy* **2019**, *4*, 123.
[16] X. Wu, Y. Qi, J. J. Hong, Z. Li, A. S. Hernandez, X. Ji, *Angew. Chem. Int. Ed.* **2017**, *56*, 13026; *Angew. Chem.* **2017**, *129*, 13206.
[17] D. Su, A. McDonagh, S. Z. Qiao, G. Wang, *Adv. Mater.* **2017**, *29*, 1604007.
[18] H. Yi, R. Qin, S. Ding, Y. Wang, S. Li, Q. Zhao, F. Pan, *Adv. Funct. Mater.* **2021**, *31*, 2006970.
[19] Q. Liu, Z. Hu, M. Chen, C. Zou, H. Jin, S. Wang, S. L. Chou, Y. Liu, S. X. Dou, *Adv. Funct. Mater.* **2020**, *30*, 1909530.
[20] Q. Li, K. Ma, G. Yang, C. Wang, *Energy Storage Mater.* **2020**, *29*, 246.
[21] Y. Tang, W. Li, P. Feng, M. Zhou, K. Wang, Y. Wang, K. Zaghib, K. Jiang, *Adv. Funct. Mater.* **2020**, *30*, 1908754.
[22] A. Zhou, Z. Xu, H. Gao, L. Xue, J. Li, J. B. Goodenough, *Small* **2019**, *15*, 1902420.
[23] Y. Shang, X. Li, J. Song, S. Huang, Z. Yang, Z. J. Xu, H. Y. Yang, *Chem* **2020**, *6*, 1804.
[24] A. Mullaliu, M. Gaboardi, J. R. Plaisier, S. Passerini, M. Giorgetti, *ACS Appl. Energy Mater.* **2020**, *3*, 5728.
[25] B. Wang, Y. Han, X. Wang, N. Bahlawane, H. Pan, M. Yan, Y. Jiang, *iScience* **2018**, *3*, 110.
[26] J. Qian, C. Wu, Y. Cao, Z. Ma, Y. Huang, X. Ai, H. Yang, *Adv. Energy Mater.* **2018**, *8*, 1702619.
[27] X. Wu, Y. Xu, C. Zhang, D. P. Leonard, A. Markir, J. Lu, X. Ji, *J. Am. Chem. Soc.* **2019**, *141*, 6338.
[28] Q. Yang, F. Mo, Z. Liu, L. Ma, X. Li, D. Fang, S. Chen, S. Zhang, C. Zhi, *Adv. Mater.* **2019**, *31*, 1901521.
[29] J. Nai, X. W. Lou, *Adv. Mater.* **2019**, *31*, 1706825.
[30] Y. Huang, M. Xie, Z. Wang, Y. Jiang, Y. Yao, S. Li, Z. Li, L. Li, F. Wu, R. Chen, *Small* **2018**, *14*, 1801246.
[31] L. Ren, J. G. Wang, H. Liu, M. Shao, B. Wei, *Electrochim. Acta* **2019**, *321*, 134671.
[32] L. Jiang, Y. Lu, C. Zhao, L. Liu, J. Zhang, Q. Zhang, X. Shen, J. Zhao, X. Yu, H. Li, X. Huang, L. Chen, Y. S. Hu, *Nat. Energy* **2019**, *4*, 495.
[33] X. Jiang, H. Liu, J. Song, C. Yin, H. Xu, *J. Mater. Chem. A* **2016**, *4*, 16205.
[34] Y. Moritomo, S. Urase, T. Shibata, *Electrochim. Acta* **2016**, *210*, 963.
[35] D. Yang, J. Xu, X. Z. Liao, Y. S. He, H. Liu, Z. F. Ma, *Chem. Commun.* **2014**, *50*, 13377.
[36] X. F. Lu, S. L. Zhang, E. Shangguan, P. Zhang, S. Gao, X. W. Lou, *Adv. Sci.* **2020**, *7*, 2001178.
[37] Y. Guo, C. Wu, N. W. Li, S. Yuan, L. Yu, *J. Mater. Chem. A* **2019**, *7*, 25247.
[38] L. Shen, L. Yu, X. Y. Yu, X. Zhang, X. W. Lou, *Angew. Chem. Int. Ed.* **2015**, *54*, 1868; *Angew. Chem.* **2015**, *127*, 1888.
[39] J. Li, L. He, J. Jiang, Z. Xu, M. Liu, X. Liu, H. Tong, Z. Liu, D. Qian, *Electrochim. Acta* **2020**, *353*, 136579.
[40] J. Wang, C. Mi, P. Nie, S. Dong, S. Tang, X. Zhang, *J. Electroanal. Chem.* **2018**, *818*, 10.
[41] Y. Zhao, B. Liang, X. Wei, K. Li, C. Lv, Y. Zhao, *J. Mater. Chem. A* **2019**, *7*, 10464.

[42] D. Wang, H. Lv, T. Hussain, Q. Yang, G. Liang, Y. Zhao, L. Ma, Q. Li, H. Li, B. Dong, T. Kaewmaraya, C. Zhi, *Nano Energy* **2021**, *84*, 105945.
[43] H. Zhang, C. Li, D. Chen, J. Zhao, X. Jiao, Y. Xia, *CrystEngComm* **2017**, *19*, 2057.
[44] C. Zhao, B. Liu, X. Li, K. Zhu, R. Hu, Z. Ao, J. Wang, *Chem. Commun.* **2019**, *55*, 7151.
[45] Y. Fang, D. Luan, Y. Chen, S. Gao, X. W. Lou, *Angew. Chem. Int. Ed.* **2020**, *59*, 7178; *Angew. Chem.* **2020**, *132*, 7245.
[46] Y. Fang, D. Luan, Y. Chen, S. Gao, X. W. Lou, *Angew. Chem. Int. Ed.* **2020**, *59*, 2644; *Angew. Chem.* **2020**, *132*, 2666.

Manuscript received: June 9, 2021
Revised manuscript received: July 19, 2021
Accepted manuscript online: July 27, 2021
Version of record online: August 31, 2021

